

## Slag Resistance Mechanism of Lightweight Microporous Corundum Aggregate

Lyping Fu,<sup>‡</sup> Huazhi Gu,<sup>‡,†</sup> Ao Huang,<sup>‡</sup> Meijie Zhang,<sup>‡</sup> and Zhengkun Li<sup>§</sup><sup>‡</sup>The State Key Laboratory of Refractories and Metallurgy, School of Materials and Metallurgy, Wuhan University of Science and Technology, Wuhan, Hubei 430081, China<sup>§</sup>The Limited Company of Jingxin High Temperature Material, Yangzhou, Jiangsu 225265, China

The microstructures of the reaction interfaces between slag and corundum aggregates, microporous corundum produced in the laboratory and tabular corundum were observed after slag resistance experiments, and their associated slag resistance mechanisms were investigated. A continuous isolation layer was observed around the microporous corundum, which showed a significantly better slag resistance than tabular corundum. The formation of columnar crystals of  $\text{CaAl}_2\text{O}_7$  ( $\text{CA}_2$ ) and  $\text{CaAl}_4\text{O}_7$  ( $\text{CA}_2$ ) in the isolation layer was the main reason for the difference in slag resistance. With respect to the nucleation and growth of second phase, the slag resistance mechanism of lightweight microporous corundum was explored by thermodynamic and kinetic analysis. Due to its smaller pore size, the second phase is more likely to achieve supersaturation, and large quantities of crystal nuclei are generated for microporous corundum. The critical dissolved depths of the microporous and tabular corundum in saturated slag were calculated to be 0.14 and 0.27  $\mu\text{m}$ , respectively. Additionally, the small pore sizes lead to an increase in the Ostwald ripening rate of the second phase, and the Ostwald ripening rate of microporous corundum was 12 times that of the tabular corundum based on Ardell's theory.

## I. Introduction

Lightweight wear lining for industrial furnaces has increasingly attracted attention in the field of refractory materials because a high-porosity lightweight wear lining could produce better heating insulation, which in turn could decrease energy consumption at high temperatures. Lightweight aggregate is a requirement for achieving lightweight wear lining refractories. Thus, lightweight aggregates have been widely investigated in recent years, and several methods have been employed to fabricate lightweight aggregates, including the decomposition of organic/inorganic matter,<sup>1–5</sup> the react bonding technique,<sup>6</sup> the pore-forming *in situ* technique,<sup>7,8</sup> and gel freeze drying.<sup>9</sup> Deng *et al.*<sup>1,2</sup> prepared alumina ceramics by the decomposition of  $\text{Al}(\text{OH})_3$ , Thijs *et al.*<sup>3</sup> produced ceramic foams with hollow spheres, and Yan *et al.*<sup>7</sup> fabricated porous corundum-mullite ceramics with  $\text{Al}(\text{OH})_3$ , kaolinite and  $\text{MgCO}_3$  as raw materials. Although the previously described lightweight aggregates exhibited positive effects on the heat-shielding performance and thermal shock resistance for wear lining refractories, high apparent porosity and large pores would weaken the slag resistance, resulting in serious corrosion of the wear lining.

Extensive studies have been carried out on the dissolution of alumina/magnesia/spinel aggregates into slag for

understanding slag resistance performance of in-service refractories wear.<sup>10–15</sup> Lee and Zhang<sup>10,11</sup> pointed out that the formation of continuous new solid phases layer would result in the indirect dissolution of refractories. Bates<sup>12</sup> observed the formation of an  $\text{MgAl}_2\text{O}_4$  (MA) spinel layer at the interface of  $\text{Al}_2\text{O}_3$  and a slag containing 10%–20%  $\text{MgO}$  at 1502°C. In addition, the corrosion of alumina and spinel in silicate slags has been investigated by Sarpoolaky *et al.*,<sup>13,14</sup> who reported that the formation of  $\text{CaAl}_2\text{O}_7$  ( $\text{CA}_2$ ) layer could prevent the refractories from slag corrosion. Nevertheless, the dissolution of lightweight microporous aggregate has not yet been investigated. In addition, several studies<sup>16,17</sup> have been reported concerning the relation between pore size and slag corrosion of refractories. Matsushita *et al.*<sup>16</sup> pointed out that slag penetration and corrosion can be modulated by microstructural control of the refractory status.

Based on the above background, the influence of pore size on slag penetration into lightweight aggregate was investigated with mathematical simulation methods by Huang *et al.*,<sup>18</sup> who pointed out that miniaturization of pore size could improve the slag resistance of lightweight aggregate. Our group prepared microporous corundum aggregates using  $\alpha\text{-Al}_2\text{O}_3$  micro-powder as the main raw material that were applied to fabricate alumina-magnesia castable.<sup>19–21</sup> Such alumina-magnesia castable exhibited excellent slag resistance in an industrial furnace. However, the intrinsic mechanism of slag resistance associated with microporous corundum aggregate is not understood, and more importantly, the relationships between porosity and pore size of the refractory and slag resistance remain unclear, as they are very important when developing new lightweight wear lining refractories with good slag resistance.

Since tabular corundum aggregates are conventionally used particles for refractory castables, they were selected as the reference substance to estimate the performance of microporous corundum aggregates. Herein, we report the slag resistance of microporous and tabular corundum aggregates for the first time following an investigation of the nucleation and growth of second phase by means of thermodynamic and kinetic analysis. A slag resistance mechanism of lightweight microporous corundum aggregate was proposed based on the Ostwald supersaturated nucleation theory and Ostwald ripening of second phase particles.

## II. Experimental Procedure

Microporous corundum was prepared as a previously published work by the authors.<sup>12</sup> In a typical synthesis,  $\alpha\text{-Al}_2\text{O}_3$  micro-powder ( $D_{50} = 2.125 \mu\text{m}$ ; Kaifeng Special Refractory Co., Ltd., Henan, China) and corn starch ( $D_{50} = 11.206 \mu\text{m}$ , Shandong Hengren Starch Co., Ltd., Shandong, China) were mixed with a mass ratio of 9:1, and then water, with approximately 50 wt% of the previously mentioned raw materials, was added to produce a slurry. The slurry was poured into the organic plastic mold, with a size of  $\Phi 40 \text{ mm} \times 50 \text{ mm}$ , after wet milling with a planetary ball mill for 30 min. The

B. Lee—contributing editor

**Table I. The Main Chemical Constituents of the Slag Composition**

Components	SiO <sub>2</sub>	Al <sub>2</sub> O <sub>3</sub>	CaO	MgO	MnO	TiO <sub>2</sub>	FeO	CaF <sub>2</sub>	Basicity (CaO/SiO <sub>2</sub> )
Mass fraction (wt%)	15.92	1.71	42.92	5.14	3.36	0.56	24.35	3.87	2.89

slurry was consolidated by the starch thermogelation after baked at 80°C for 24 h and then demolded. The samples were dried at 110°C for 24 h and heated at 1830°C for 3 h, and the microporous corundum was then produced.

Tabular corundum aggregates (99.5 wt% Al<sub>2</sub>O<sub>3</sub>, 0.15 wt% Na<sub>2</sub>O, 0.08 wt% Fe<sub>2</sub>O<sub>3</sub>, 0.06 wt% SiO<sub>2</sub>) were produced and supplied by Jiangsu Jingxin High-temperature Materials Co., Ltd., Jiangsu, China. The particle size distribution was measured by sieve analysis, and its  $D_{50}$  was measured as 13.1 μm.

The bulk density and apparent porosity of corundum aggregates were determined by the Archimedes' Principle with water as the medium. True density was measured using automatic true density analyzer (ACCUPYC 1330; Micromeritics Instrument Corporation, Norcross, GA). The closed porosity of samples could be calculated from the Eqs. (1) and (2).

$$\pi_t = \frac{\rho_t - \rho_b}{\rho_t} \times 100\% \quad (1)$$

$$\pi_c = \pi_t - \pi_a \quad (2)$$

where,  $\pi_t$  is the total porosity;  $\rho_t$  is the true density;  $\rho_b$  is the bulk density;  $\pi_a$  is the apparent porosity;  $\pi_c$  is the closed porosity.

The pore size distribution and average pore diameter of different corundum aggregates were measured by mercury intrusion porosimetry measurements (AutoPore IV 9500; Micromeritics Instrument Corporation).

The corundum materials obtained after sintering were ground by a jaw crusher (PEX-60×100; Zhejiang Fute Machinery Co., Ltd., Zhejiang, China.). Laboratory-produced microporous and tabular corundum aggregates with diameters of approximately 12 mm were chosen as raw materials for this study. To guarantee the accuracy of the experimental results, two samples of each type were tested. Corundum aggregates were put into an alumina crucible together with a converter slag (<0.088 mm; Wugang Refractory Co., Ltd., Wuhan, China). The composition of the slag is shown in Table I. The weight ratio of slag to corundum was approximately 3:1. The alumina crucibles (with corundum aggregates and slag inside) were put into a box furnace and then heated at a rate of 7°C/min up to 1600°C. After annealing at 1600°C for 3 h, the alumina crucibles were cooled to room temperature and then cut open by a cutting machine (QG-2; Shanghai Zhongheng Instrument Co. Ltd., Shanghai, China). Samples after corrosion test were separated perpendicular to the corundum/slag interface, embedded and fixed in cold-setting resin. Standard grinding and polishing techniques (the smallest abrasive grain used in this study was 3.5 μm) were used then, after which all samples were coated with gold. The microstructures and composition of the samples were characterized by scanning electron microscopy (SEM; JSM-6610, JEOL, Tokyo, Japan) and an attached X-ray energy dispersive spectroscopy (EDX; QUANTAX, Bruker, Berlin, Germany).

### III. Results and Discussion

#### (1) Performances of Aggregates

Tabular corundum aggregate was chosen as a control to investigate the performance of the microporous corundum

**Table II. Performance Parameters of Different Corundum Aggregates<sup>21</sup>**

Corundum aggregate	Bulk density (g/cm <sup>3</sup> )	True density (g/cm <sup>3</sup> )	Apparent porosity (%)	Closed porosity(%)
Tabular corundum	3.63	3.94	2.8	5.0
Microporous corundum	3.36	3.92	4.1	10.1

aggregate produced in the laboratory. Herein, the performances of the two corundum aggregates are compared.

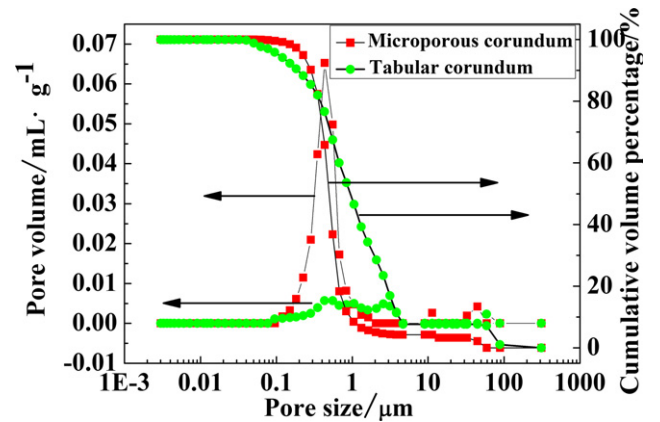
Table II shows the density and porosity of different corundum aggregates. It can be seen that the microporous corundum shows a lower bulk and true density compared to the tabular corundum. Although there is a slight increase in the apparent porosity, the closed porosity of microporous corundum is significantly higher, about twice as much as that of tabular corundum.

Microporous corundum has a narrower pore size distribution than that of tabular corundum, as suggested by Fig. 1. In addition, the pore distribution of microporous corundum exhibits a single and relatively centered peak with most of the pore sizes below 1 μm. However, the pore size distribution of tabular corundum shows a larger range, which is centered on the values of 1–5 μm. In addition, the median pore diameters of microporous corundum and tabular corundum are 0.49 and 0.95 μm, respectively.

#### (2) Microstructure and Analysis

We further investigated the reaction interface between the aggregates and the slag to compare the slag resistance of the two different corundum aggregates.

Figure 2 shows typical SEM images of tabular aggregates after the slag resistance experiment. Figure 2(a) indicates that columnar crystals distributed around the aggregate, which were determined to be CaAl<sub>12</sub>O<sub>19</sub> (CA<sub>6</sub>) and CaAl<sub>4</sub>O<sub>7</sub> (CA<sub>2</sub>) by EDX attached to the SEM. The CA<sub>6</sub> and CA<sub>2</sub> layer has heterogeneous thickness around 20–50 μm. In addition, slag penetrates into the aggregate through gaps between crystals, and it severely corrodes the aggregate [Fig. 2(b)]. Moreover, the slag penetrates into aggregates mainly through large pores and cracks, and the penetration around small pores is

**Fig. 1. Pore size distribution of different corundum aggregates.**

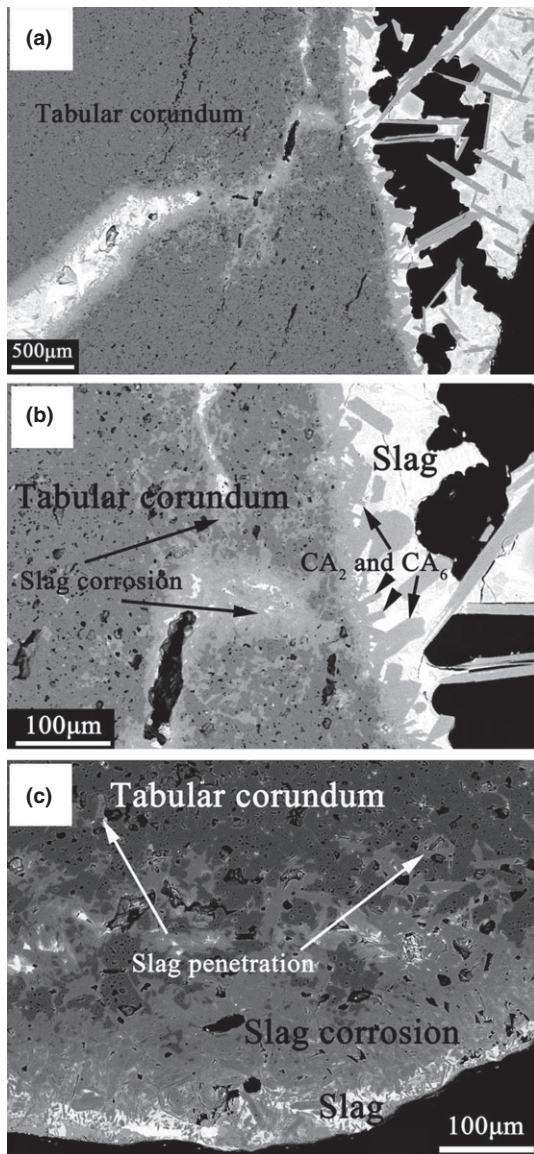


**Fig. 2.** SEM images of the reaction interface between slag and tabular corundum aggregate: (a) a small amount of columnar crystals distributed around the aggregate; (b) higher magnification of (a); (c) partial slag-penetrated region without columnar crystals.

weak. Our results also indicate that the slag significantly penetrated into the aggregate at partial slag-penetrated region without the columnar crystals, as indicated by Fig. 2(c). These results prove that the tabular corundum exhibits poor slag resistance.

Figure 3 shows the SEM images of the interface after microporous corundum aggregates were corroded by the slag. A continuous isolation layer with a thickness of 50–100  $\mu\text{m}$  is formed on the surface of microporous corundum [Fig. 3(a)]. In addition, a larger number of columnar crystals, when compared to tabular corundum, were distributed in the isolation layer, and the growth direction of these columnar crystals is perpendicular to the surface of the microporous corundum aggregates. Spinel [ $\text{Mg}(\text{Al}, \text{Mn}^{3+}, \text{Fe}^{3+})_2\text{O}_4$ ] crystals are also observed among the columnar crystals of  $\text{CA}_6$  and  $\text{CA}_2$ , as suggested by the EDX results shown in Fig. 3(b). When the aggregates are exposed to the slag, the  $\text{CaO}$  in the slag will react with corundum first to form high melting point phases such as  $\text{CA}_6$  and  $\text{CA}_2$ . Since the  $\text{CaO}$  is largely consumed, the viscosity of the slag increases. The decrease in  $\text{Ca}$  concentration in slag favored the local increase in the amount of  $\text{Mg}$ , which reacted with  $\text{Al}_2\text{O}_3$  to form spinel. Additionally,  $\text{Fe}_x\text{O}$  and  $\text{MnO}$  were

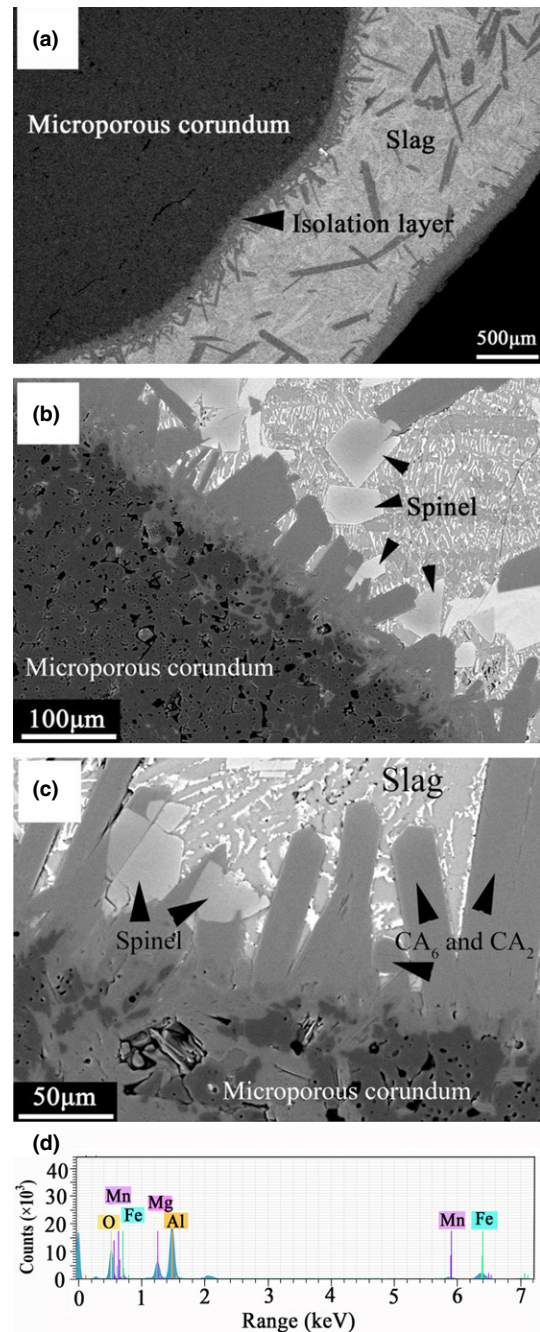


**Fig. 3.** SEM images of the reaction interface between slag and microporous corundum aggregate: (a) a continuous isolation layer is formed on the surface of microporous corundum; (b) and (c) higher magnification of (a); (d) EDX spectrum of the spinel.

absorbed by spinel during the reaction. The consequent increase in viscosity also favors the local concentration of reactants. An isolated layer was formed *in-situ* with the generation of numerous calcium aluminates and spinel, and effectively prevented the sample from further corrosion and from slag penetrating into the aggregate; hence, the aggregate was slightly corroded compared to the seriously corroded tabular corundum.

### (3) Thermodynamic and Kinetic Analysis

The above-mentioned results indicated that the columnar crystals play an important role in the slag resistance of lightweight microporous corundum aggregate. Hence, the nucleation and growth of crystals were investigated to explore the related slag resistance mechanism.

(A) *Nucleation of the Second Phase:* According to Ostwald's supersaturation theory,<sup>22</sup> nucleation free energy depends on the supersaturation of the solution (S), net interfacial energy of nucleation ( $\sigma$ ), temperature ( $T$ ), and superficial area of grains ( $A$ ):

$$\Delta G = -T \ln S + \sigma A \quad (3)$$

According to Eq. (3), increasing the supersaturation of the solution is conducive to nucleation of the second phase.

In this study, since columnar crystals are mainly composed of CaO and Al<sub>2</sub>O<sub>3</sub>, assuming that CaO is the matrix and Al<sub>2</sub>O<sub>3</sub> is the second phase. In the following parts, the dissolution and supersaturated precipitation of Al<sub>2</sub>O<sub>3</sub> in CaO are discussed.

The slag resistance experiment was carried out at 1600°C in this study. As shown in Fig. 4, theoretically, solid phases (CA<sub>2</sub>) appear at this temperature when the mass ratio of Al<sub>2</sub>O<sub>3</sub> and CaO is 1.82. This means that when the mass ratio is greater than 1.82, the slag is supersaturated and calcium aluminates will precipitate out.

Considering the difference between the two samples stands in pore size and porosity of the aggregates, the observed difference in slag resistance of the two samples is mainly caused by the relation between pores and slag penetration. When the aggregates are exposed to the slag, the pores, which are the weakest parts, are the first to be penetrated by the slag. Assuming that the voids in the aggregates are of spherical shape and that the slag penetration along each direction in the two aggregates occurs at the same rate, the mass ratio of Al<sub>2</sub>O<sub>3</sub> and CaO in each pore can be calculated from Eq. (4):

$$\omega = \frac{\left[ \frac{2}{3} \pi (x+r)^3 - \frac{2}{3} \pi (r)^3 \right] \rho_a + \frac{2}{3} \pi (x+r)^3 \rho_s \omega_{Al_2O_3}}{\frac{2}{3} \pi (x+r)^3 \rho_s \omega_{CaO}} \times 100\% \quad (4)$$

where  $\omega$  is the mass ratio of Al<sub>2</sub>O<sub>3</sub> and CaO,  $x$  is the dissolved depth of the aggregate in slag,  $r$  is the radius of the pore,  $\rho_a$  is the true density of the aggregate,  $\rho_s$  is the density of the slag, and  $\omega_{Al_2O_3}$  and  $\omega_{CaO}$  are the mass fraction of Al<sub>2</sub>O<sub>3</sub> and CaO in slag, respectively.

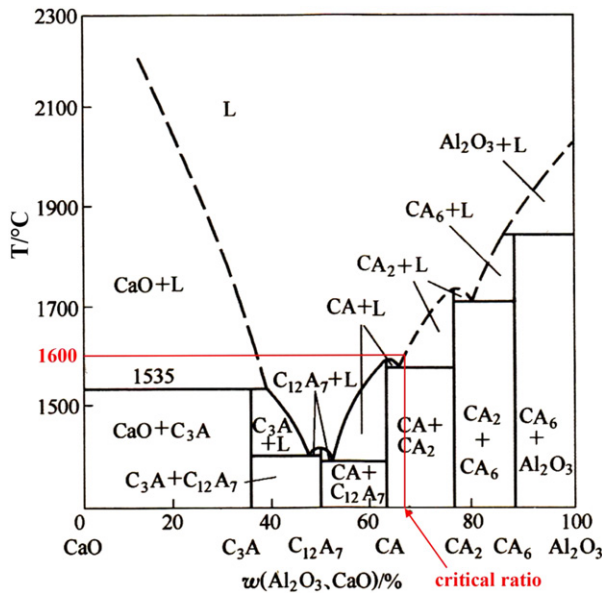


Fig. 4. CaO–Al<sub>2</sub>O<sub>3</sub> phase diagram.

Table III. The Densities of Compounds in the Slag (wt%)

Compounds	SiO <sub>2</sub>	Al <sub>2</sub> O <sub>3</sub>	CaO	MgO	MnO	TiO <sub>2</sub>	FeO	CaF <sub>2</sub>
Density (g/cm <sup>3</sup> )	2.32	3.97	3.32	3.59	5.40	4.24	5.9	2.8

The true densities of the aggregates are listed in Table II. The density of the slag can be estimated using Eq. (5)<sup>23,24</sup>:

$$\rho_s = \sum_{i=1}^n (\rho_i \omega_i) \quad (5)$$

where  $\rho_i$  and  $\omega_i$  are the density and mass fraction of compounds in the slag, respectively. The values for the densities of the compounds in the slag are listed in Table III, while the mass fractions are listed in Table I. The calculated value for  $\rho_s$  is equal to 3.797 g/cm<sup>3</sup>.

The median pore diameters of microporous and tabular corundum are 0.49 and 0.95 μm (Fig. 1), respectively. Thus, the radii of the pores are 0.245 and 0.475 μm, respectively. Introducing these values into Eq. (4), the calculation indicates that when the slag reaches its saturation point, the critical dissolved depths of 0.14 and 0.27 μm are obtained for microporous and tabular corundum, respectively. In fact, the pore size distribution of tabular corundum is centered on the values of 1–5 μm. That distribution indicates the critical dissolved depth of tabular corundum in slag is actually much larger than 0.27 μm.

Hence, due to the smaller pore size of microporous corundum aggregate, the second phase is more likely to achieve supersaturation when the aggregate reacts with the slag, and massive crystal nuclei are immediately generated.

(B) *Growth of the Second Phase:* When the precipitation is completed, the conglomeration and growth of the second phase, called Ostwald ripening, will occur instantly.

The solute concentration around small, second phase particles is greater than that around large particles; hence, solute atoms will diffuse from small crystals to large crystals. The diffusion will break the balance of solute concentration around the crystals, and then it will result in the dissolution of small particles and growth of large particles. Therefore, average particle size will increase. This is the Ostwald ripening process.

The main driving force of Ostwald ripening is due to the concentration gradient between particles. The greater the concentration gradient is, the higher the rate of Ostwald ripening. The quasi-stability concentration gradient between second phase particles and the matrix interface can be calculated from Eq. (6):<sup>25,26</sup>

$$\left. \frac{\partial C}{\partial R} \right|_{R=r} = \frac{C'_r - C}{r(1 - \frac{r}{r'})} \quad (6)$$

where  $C'_r$  is the actual concentration of solute in the matrix,  $C$  is the quasi-stability mean concentration of solute in the matrix,  $r$  is the particle radius of second phase, and  $r'$  is the spacing between two second phase particles.

The spacing between two second phase particles decreases when the volume fraction of the second phase increases. As a result, the quasi-stability concentration gradient between the second phase particles and the matrix interface increases [as shown in Eq. (6)] and, consequently, the rate of the Ostwald ripening increases.

In this experiment, the pore size of microporous corundum aggregate is smaller than that of tabular corundum; hence, the volume fractions of the second phase and the Ostwald ripening rate of high melting point phases increase, and there

is growth of columnar crystals. In the following section, the difference between the Ostwald ripening rates of the two previously mentioned corundum aggregates is calculated.

The volume fraction of the second phase can be determined using Eq. (7):

$$\varphi = (M - [M]) \frac{\rho_m}{\rho_M} \times 100\% \quad (7)$$

where  $\varphi$  is the volume fraction of the second phase,  $M$  is the mass ratio of the second phase to the matrix,  $[M]$  is the mass ratio of second phase dissolved in the matrix, and  $\rho_m$  and  $\rho_M$  are the density of the matrix and second phase, respectively.

As shown in Section [III(3)(B)], the slag is saturated when the dissolved depth of tabular corundum in the slag is 0.27  $\mu\text{m}$ . When the dissolved depth of the microporous corundum reaches this same value, the mass ratio of  $\text{Al}_2\text{O}_3$  and  $\text{CaO}$  equals 2.19, as calculated from Eq. (4). Introducing these parameters into Eq. (7), the volume fraction of the second phase when microporous corundum reacts with the slag is:

$$\varphi = (M_{\text{Al}_2\text{O}_3} - [M_{\text{Al}_2\text{O}_3}]) \frac{\rho_{\text{CaO}}}{\rho_{\text{Al}_2\text{O}_3}} \times 100\% = 0.309 \quad (8)$$

The reaction between the refractory and slag is controlled by diffusion. The Ostwald ripening rate of reactions controlled by diffusion has been investigated by Ardell.<sup>27</sup> The influence of the volume fraction on the Ostwald ripening rate can be determined using Eq. (9–13):

$$p_\varphi = \frac{k_{1\varphi}^{-3} \lambda_1}{\lambda_{1\varphi}} \quad (9)$$

$$\gamma_{1\varphi} = \frac{\rho_{1\varphi \max}^2}{1 + 2\beta \rho_{1\varphi \max} - \beta} \quad (10)$$

$$\rho_{1\varphi \max} = \frac{\sqrt{\beta^2 + \beta + 1} - (1 - \beta)}{\beta} \quad (11)$$

$$\beta = \frac{6\varphi^{1/3}}{\exp \varphi \Gamma(1/3, \varphi)} \quad (12)$$

$$\Gamma(1/3, \varphi) = \int_\varphi^\infty x^{-2/3} e^{-x} dx \quad (13)$$

where  $p_\varphi$  indicates the increased multiple of the Ostwald ripening rate caused by the volume fraction of the second phase,  $\varphi$ ;  $\gamma_{1\varphi}$ ,  $\rho_{1\varphi \max}$ , and  $\beta$  are intermediate parameters; and  $\gamma_1$  is equal to 9/4 and  $k_{1\varphi}^{-3} = 0.913$  when  $\varphi$  is 0.309.

Introducing the results of Eq. (8) into Eq. (9–13), it follows that  $p_\varphi$  is equal to 12. This indicates that, according to Ardell's theory, the Ostwald ripening rate of microporous corundum is 12 times that of tabular corundum in the reaction with the slag.

#### (4) Slag Resistance Mechanism

Figure 5 shows the reaction between the different corundum aggregates and the molten slag. During the reaction between the slag and corundum aggregate, slag penetration into aggregate pores result in the formation of  $\text{CaO-Al}_2\text{O}_3$  system phases. Due to the smaller pore sizes of the microporous corundum aggregate, the second phase is more likely to achieve supersaturation during the reaction between the aggregate and slag, and large quantities of crystal nuclei are immediately generated. In addition, the small pore sizes increase the second phase volume fraction and the Ostwald ripening rate of crystal nuclei, and the columnar crystals grow. These high melting point phases of  $\text{CA}_2$  and  $\text{CA}_6$  are distributed around the aggregate and an isolation layer adheres to the hot face of the aggregate, thus effectively preventing further corrosion and penetration by the slag.

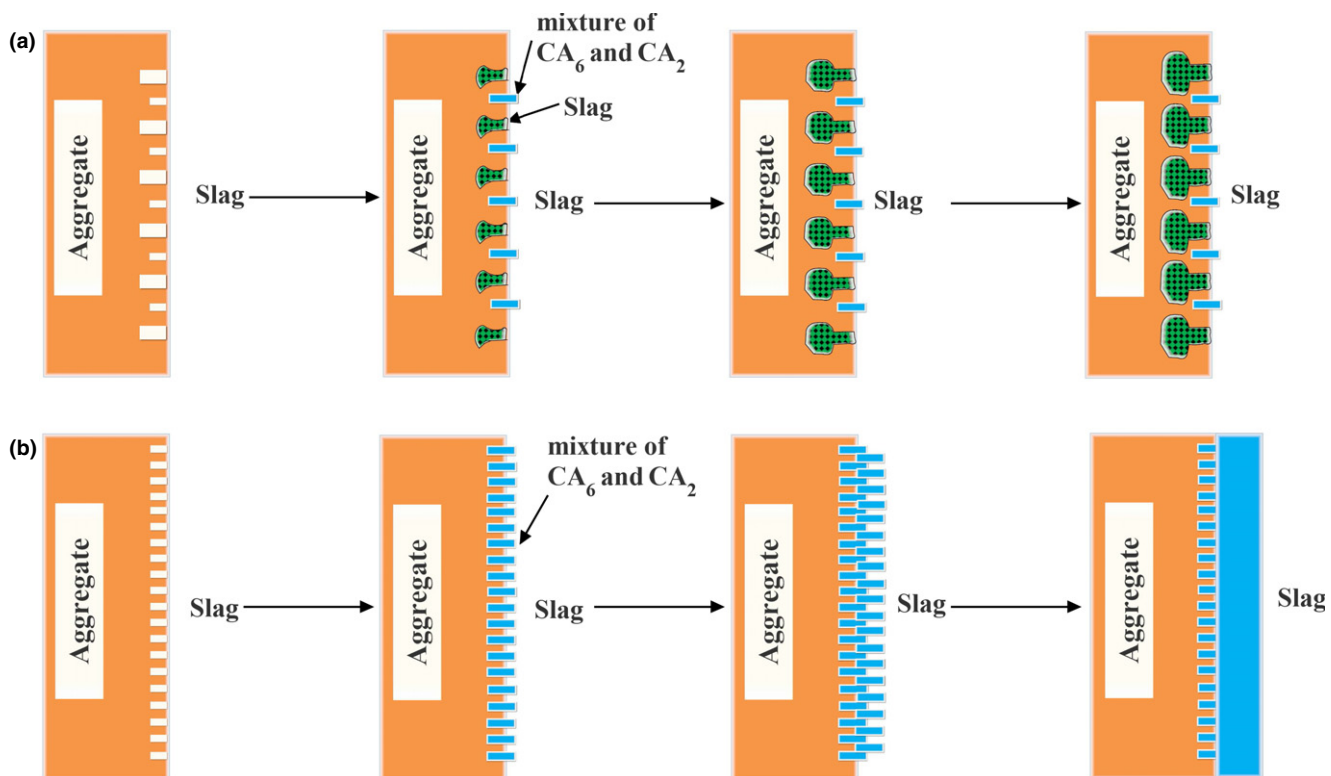


Fig. 5. Schematic diagram of the reaction between molten slag and (a) tabular corundum, and (b) lightweight microporous corundum.

However, as shown in Fig. 1, approximately 70% of the pores in tabular corundum aggregate are larger than 1  $\mu\text{m}$ ; consequently, crystal nuclei of the second phase are difficult to generate and grow. The aggregate is then further corroded.

#### IV. Conclusions

The slag resistance of lightweight microporous corundum aggregate, whose median pore diameter is 0.49  $\mu\text{m}$ , was significantly better than that of the tabular corundum aggregate. Microstructure and energy spectrum analyses show that the formation of columnar crystals of  $\text{CA}_2$  and  $\text{CA}_6$ , is the main reason for the observed difference in slag resistance. The columnar crystals, which are distributed around the aggregate, prevented the aggregate from further corrosion and from slag penetration.

Due to the smaller pore sizes of the microporous corundum aggregate, the second phase is more likely to achieve supersaturation, and large quantities of crystal nuclei are immediately generated. In addition, the small pore size leads to an increase in the second phase volume fraction and the Ostwald ripening rate of high melting point phase formations, and the crystal nuclei grow immediately. When the slag is saturated, the critical dissolved depth of microporous and tabular corundum in the slag were calculated to be 0.14 and 0.27  $\mu\text{m}$ , respectively. Moreover, according to Ardell's theory, the Ostwald ripening rate of microporous corundum was 12 times that of tabular corundum. Our results reveal the relationships between porosity and pore size of the refractory and slag resistance and slag resistance associated with microporous corundum aggregate, which are very important for developing new lightweight wear lining refractories with good slag resistance.

#### Acknowledgments

This work was financially supported by the National Natural Science Foundation of China (grant nos. 51474165 and 51204126) and the National Basic Research Program of China (grant no. 2012CB 722702).

#### References

- <sup>1</sup>Z. Deng, T. Fukasawa, and M. Ando, "High-Surface-Area Alumina Ceramics Fabricated by the Decomposition of  $\text{Al}(\text{OH})_3$ ," *J. Am. Ceram. Soc.*, **84** [3] 485–91 (2001).
- <sup>2</sup>Z. Deng, T. Fukasawa, and M. Ando, "Microstructure and Mechanical Properties of Porous Alumina Ceramics Fabricated by the Decomposition of Hydroxide," *J. Am. Ceram. Soc.*, **84** [1] 2638–44 (2001).
- <sup>3</sup>I. Thijs, J. Luyten, and M. Steven, "Producing Ceramic Foams with Hollow Spheres," *J. Am. Ceram. Soc.*, **87** [1] 170–2 (2003).
- <sup>4</sup>F. Tang, H. Fudouzi, and Y. Sakka, "Fabrication of Macroporous Alumina with Tailored Porosity," *J. Am. Ceram. Soc.*, **86** [12] 2050–4 (2003).
- <sup>5</sup>R. Salomão, M. V. Bôas, and V. C. Pandolfelli, "Porous Alumina-Spinel Ceramics for High Temperature Applications," *Ceram. Int.*, **37** [4] 1393–9 (2011).
- <sup>6</sup>J. H. She and T. Ohji, "Fabrication and Characterization of Highly Porous Mullite Ceramics," *Mater. Chem. Phys.*, **80** [3] 610–4 (2003).
- <sup>7</sup>W. Yan, N. Li, and B. Q. Han, "Effects of Sintering Temperature on Pore Characterization and Strength of Porous Corundum-Mullite Ceramics," *J. Ceram. Process. Res.*, **11** [3] 388–91 (2010).
- <sup>8</sup>S. J. Li and N. Li, "Effects of Composition and Temperature on Porosity and Pore Size Distribution of Porous Ceramics Prepared from  $\text{Al}(\text{OH})_3$  and Kaolinite Gangue," *Ceram. Int.*, **33** [4] 551–6 (2007).
- <sup>9</sup>S. Q. Ding, Y. P. Zeng, and D. L. Jiang, "Fabrication of Mullite Ceramics with Ultrahigh Porosity by Gel Freeze Drying," *J. Am. Ceram. Soc.*, **90** [7] 2276–9 (2007).
- <sup>10</sup>W. E. Lee and S. Zhang, "Melt Corrosion of Oxide and Oxide-Carbon Refractories," *Int. Mater. Rev.*, **44** [3] 77–104 (1999).
- <sup>11</sup>S. W. Zhang, H. R. Rozaie, and H. Sarpoolaky, "Alumina Dissolution into Silicate Slag," *J. Am. Ceram. Soc.*, **83** [4] 897–903 (2000).
- <sup>12</sup>J. L. Bates, "Heterogeneous Dissolution of Refractory Oxides in Molten Calcium-Aluminum Silicates," *J. Am. Ceram. Soc.*, **70** [3] 55–7 (1987).
- <sup>13</sup>H. Sarpoolaky, S. Zhang, B. B. Argent, and W. E. Lee, "Influence of Grain Phase on Slag Corrosion of Low-Cement Castable Refractories," *J. Am. Ceram. Soc.*, **84** [2] 426–34 (2001).
- <sup>14</sup>H. Sarpoolaky, S. Zhang, and W. E. Lee, "Corrosion of High Alumina and Near Stoichiometric Spinels in Iron-Containing Silicate Slags," *J. Eur. Ceram. Soc.*, **23** [2] 296–300 (2003).
- <sup>15</sup>K. H. Sandhage and G. J. Yurek, "Direct and Indirect Dissolution of Sapphire in Calcia-Magnesia-Alumina-Silica Melts: Electron Microprobe Analysis of the Dissolution Process," *J. Am. Ceram. Soc.*, **73** [12] 3643–9 (1990).
- <sup>16</sup>T. Matsushita, T. Ohuchi, K. Mukai, I. Sasaka, and J. Yoshitomi, "Direct Observation of Molten Steel Penetration into Porous Refractory," *J. Tech. Assoc. Refract. Jpn.*, **23** [1] 15–9 (2003).
- <sup>17</sup>T. K. Kaneko, J. X. Zhu, and N. Howell, "The Effects of Gasification Feedstock Chemistries on the Infiltration of Slag into the Porous High Chromia Refractory and Their Reaction Products," *Fuel*, **115**, 248–63 (2014).
- <sup>18</sup>A. Huang, H. Z. Gu, and Y. Zou, "Towards Efficient Modeling on Slag Corrosion of Lightweight Corundum Spinel Castable for Ladle"; (Paper No. 17-06) presented at the 13th Unified International Technical Conference on Refractories (UNITECR), Victoria, BC, CA, September 10, 2013.
- <sup>19</sup>Y. Zou, H. Z. Gu, A. Huang, M. J. Zhang, and C. Ji, "Effect of  $\text{MgO}$  Micropowder on Microstructure and Resistance Coefficient of  $\text{Al}_2\text{O}_3$ - $\text{MgO}$  Castable Matrix," *Ceram. Int.*, **40** [5] 7023–8 (2014).
- <sup>20</sup>H. Z. Gu, L. P. Fu, L. Y. Ma, X. Gao, Y. Zhao, and B. Du, "Preparation of Microporous Corundum Aggregates and Their Applications in Lightweight Alumina-Magnesia Castables," *Refract. Man.*, **63** [3] 121–4 (2014).
- <sup>21</sup>L. P. Fu, H. Z. Gu, A. Huang, M. J. Zhang, X. Q. Hong, and L. W. Jin, "Possible Improvements of Alumina-Magnesia Castable by Lightweight Microporous Aggregates," *Ceram. Int.*, **41** [1] 1263–70 (2015).
- <sup>22</sup>T. D. Mitchell and L. C. Jonghe, "Processing and Properties of Particulate Composites from Coated Powders," *J. Am. Ceram. Soc.*, **78** [1] 199–204 (1995).
- <sup>23</sup>Y. Bottinga and D. F. Weill, "Densities of Liquid Silicate Systems Calculated From Partial Molar Volumes of Oxide Components," *Am. J. Sci.*, **269** [2] 169–82 (1970).
- <sup>24</sup>K. C. Mills and B. J. Keene, "Physical Properties of BOS Slags," *Int. Mater. Rev.*, **32** [1] 1–120 (1987).
- <sup>25</sup>A. D. Brailsford and P. Wynblatt, "The Dependence of Ostwald Ripening Kinetics on Particle Volume Fraction," *Acta Metall.*, **27**, 489–97 (1979).
- <sup>26</sup>C. K. L. Davis, P. Nash, and R. N. Stevens, "The Effect of Volume Fraction of Precipitate on Ostwald Ripening," *Acta Metall.*, **28**, 179–89 (1980).
- <sup>27</sup>A. J. Ardell, "The Effect of Volume Fraction on Particle Coarsening: Theoretical Consideration," *Acta Metall.*, **20**, 61–71 (1972). □